Transient thermal modeling of a liquid-tin solar tubular reactor for methane pyrolysis hydrogen production

Elisa Alonso[a], Alessandro Gallo[b] and Alberto Abánades[c]

[a] *Universidad Politécnica de Madrid, ETSII, TE4S Group, Spain, elisa.alonso@upm.es*
[b] *Universidad Politécnica de Madrid, ETSIDI, TE4S Group, Spain, alessandro.galloso@upm.es*
[c] *Universidad Politécnica de Madrid, ETSII, TE4S Group, Spain, alberto.abanades@upm.es*

Abstract:

Methane pyrolysis is a promising pathway for low-carbon hydrogen production, as it enables the generation of hydrogen without direct CO_2 emissions while producing solid carbon as a valuable by-product. Among the different technological options, liquid-metal reactors offer significant advantages in terms of thermal management and solid carbon handling. In parallel, concentrating solar thermal (CST) technology provides a renewable and scalable source of high-temperature heat suitable for this highly endothermic process.

In this work, a transient thermal-reactive model is developed to analyse the operation of a liquid-tin tubular reactor for methane pyrolysis integrated into a solar tower cavity receiver. Methane is injected at the bottom of silicon carbide tubes and bubbled through molten tin, where it is rapidly heated and decomposed into hydrogen and solid carbon. A one-dimensional axial model is implemented, accounting for transient heat transfer, solar irradiation, thermal losses, and first-order reaction kinetics. Radial temperature gradients within the tube are neglected based on a fin analysis of the tube cross-section, which demonstrates near-isothermal behaviour due to the high thermal conductivity of liquid tin.

The model is applied to a 2 MW_{th} solar receiver composed of 150 tubes, and three different axial solar flux distributions are investigated: bell-shaped, flat, and peaked. Results show that the molten tin effectively homogenises radial temperatures, while the axial solar flux distribution strongly influences the thermal response, methane conversion, and hydrogen production rate. Flat and bell-shaped flux profiles lead to more uniform axial temperatures and stable hydrogen production, whereas peaked distributions induce local thermal maxima and higher instantaneous production at the expense of larger axial gradients.

The results suggest the technical feasibility of integrating liquid-tin methane pyrolysis reactors into CST systems and highlight the importance of solar flux management for achieving stable and efficient hydrogen production under transient solar conditions.

Keywords:

Methane pyrolysis, liquid-metal reactor, solar thermal hydrogen production, transient thermal modelling

1. Introduction

Currently, around 96% of hydrogen is produced from fossil fuels, mainly by steam reforming of natural gas (SMR) [1] with a low cost ranging in 0.27 to 1.6 \$/kgH_2 [2] significant CO_2/CO emissions of 10-12 kg CO_2-equivalent (CO_2-eq)/kgH_2 [3]. The remaining 4 % comes from water electrolysis which is still very expensive (between 3.5 and 5.8 \$/kg H_2 [4]), involves extensive water consumption and a requires the use of critical rare earth metals.

Methane pyrolysis is an alternative hydrogen production process that has been known since almost a century [5]. This process, which also produces high-value carbon (carbon black or graphite) as a co-product, has been a subject of research interest ever since. In the 1980s and 1990s a significant body of literature was published about methane pyrolysis, having relevance the publications of Steinberg and co-workers [6–8]. The process consists in dissociating the methane molecules (CH_4) into hydrogen (H_2) and high purity solid carbon (C) according to:

$$CH_4 \rightarrow C + 2H_2 \qquad \Delta H_{298K} = 74.9 \text{ kJ/mol}$$

The reaction co-product, carbon, is currently one of the top 50 global commodities, with a market valued at 20.6 billion € in 2023 and is a critical raw material likely to become more stressed by the demand of traditional industries, as steel manufacturing, and more recent technologies as graphene, or Li-ion batteries. The demand of carbon materials, in particular graphite, will be multiplied by a factor 14, from 250 kt/year to 3.5 Mt/year in 2050 [9].

Pyrolysis avoids the generation of CO_2 or CO emissions as the carbon atoms present in methane are transformed into solid carbon. This is the main advantage of this method over other thermal processes starting from fossil fuels. Different sources of energy can supply the dissociation enthalpy required by the endothermic reaction. The utilization of a plasma-arc is the most developed option up to now [10]. Plasma-based processing is at a high Technology Readiness Level (TRL) stemming from decades of research but exhibits a low energy efficiency [11]. Moreover, these processes need to face technological issues related to the electrostatic deposition of carbon particles in the electrodes resulting in significant operation and maintenance expenses. Complementary energy supply options include driving the pyrolysis with microwave radiation that generates high energy electrons, which in turn initiate methane pyrolysis, reducing the energy requirements of the process [12]

As methane pyrolysis relies on heating methane to high temperatures, a common issue in typical gas-phase reactors is carbon deposition on walls and ducts, leading to undesired blockages [13,14]. Catalysed pyrolysis is an alternative that reduces the required temperature. The identification of suitable metallic and carbonaceous catalysts has been widely studied [15,16]. The challenge in this case is the design of a continuous device that could be used at industrial scale. Nickel could be applied as catalyst to perform the reaction between 500 and 700 °C but the generated carbon deactivates the catalyst quickly. Regeneration by combustion would annihilate carbon recovery and lead to undesired CO_2 emissions. Economically, catalysed pyrolysis is not favoured because of complexity and cost by the catalyst management [17].

Methane decomposition in liquid reaction media has been proposed as a potential alternative technology for practical industrial implementation [18]. Its main advantage is a simplified management of the carbon particles into the reactor via flotation: carbon particles naturally rise to the top of the reactor owing to the difference in density with the liquid bath [19–21]. Carbon can then be mechanically recovered from the reactor top and exploited as a high-value co-product, thereby depositions and blockages are avoided. Performing the reaction in liquid medium effectively removes oxygen from the process without the need to use any sweeping gas. Additionally, when the liquid medium consists of a metal bath, it significantly enhances the thermal management of the system. The high thermal conductivity of the metal ensures good temperature uniformity throughout the reaction medium, which is essential for achieving consistent performance and is a critical factor for the successful scalability of the process. Tin, in particular, is regarded as an excellent liquid metal for high-temperature thermal processes because of its high boiling point and thermal conductivity [22]. Methane can be bubbled through a columnar reactor where tin is in molten state and at high temperature. In this way, methane bubbles heat up rapidly and split into hydrogen and carbon. The resulting carbon accumulates at the surface of the tin, while hydrogen ascends and it is collected from the reactor top [23–26].

Concentrating solar thermal (CST) technology provides a versatile and renewable energy source capable of delivering the high-temperature heat required by the methane pyrolysis among other numerous industrial process [27]. The current trend in concentrating solar thermal (CST) technology is to push the boundaries of operating temperatures through the development of advanced systems, such as third-generation central receiver plants and innovative receiver materials [28]. These efforts aim to enable CST to deliver thermal energy at levels well above 700°C and even up to 1500°C, addressing the increasing demand for high-temperature heat in industrial processes and maximizing overall system efficiency [29]. Consequently, the capability of modern CST systems to achieve such elevated temperatures positions them as a highly suitable and attractive thermal energy source for methane pyrolysis [30–32].

Unlike conventional methane, biomethane originates from renewable sources, primarily through the anaerobic digestion and subsequent upgrading of biogas generated from agricultural residues, [33], animal manure [34,35] municipal solid waste [36], and wastewater treatment by-products [37,38]. The use of biomethane as a feedstock not only harnesses the energy potential of otherwise underutilized organic waste streams but also embeds the process within a circular economy framework, supporting both resource efficiency and greenhouse gas mitigation. In recent years, advancements in conversion and purification technologies have enabled the large-scale production of high-purity biomethane [39,40]. By integrating biomethane into hydrogen production via pyrolysis, it becomes possible to develop carbon-neutral or even carbon-negative value chains, thereby reinforcing the broader goals of renewable energy deployment and climate action.

In this work, a transient thermal-reactive model is proposed to estimate the operation of a liquid-tin (bio)methane pyrolysis reactor integrated into a concentrating solar thermal receiver. In the proposed configuration, (bio)methane is bubbled through a molten tin reactor, promoting its decomposition into hydrogen

and solid carbon. The reactor is integrated into a solar tower facility, with a field of heliostats focusing solar radiation onto a cavity receiver that houses the liquid metal reactor. The objective of the model is to analyse the viability of the concept.

2. System description

The proposed system comprises a tower-based solar plant equipped with a cavity receiver, on the rear wall of which a series of silicon carbide (SiC) tubular reactors are mounted. These reactors are exposed to concentrated radiative flux over one-third of their circumferential surface area —specifically, the sector oriented toward the aperture [41]. The remainder of each tube perimeter is thoroughly insulated, thereby approximating an adiabatic boundary condition.

For the purposes of this study, the receiver is designed with a nominal thermal power output P= 2 MW distributed among N=150 identical tubes. P and N fix the nominal methane mass flow rate per tube as the overall thermal power divided by the number of tubes and the reaction enthalpy of methane splitting (ΔH_{CH4} = 5679 kJ/kgCH_4). Inside each tube, one-fourth of the volume is occupied by methane bubbles flowing through the molten tin (assumed constant for simplicity), while the remaining three-fourth are filled with liquid tin.

The cavity is open to the surroundings through a frontal aperture. Figure 1 shows a schematic representation of the solar plant and cavity receiver with an aperture of area A_{ap} with the SiC tubes internally filled with tin and methane bubbles for illustrative purposes.

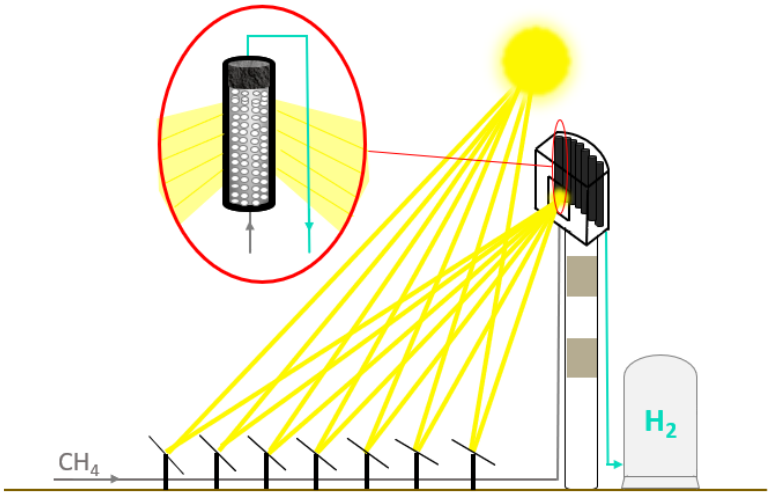

Figure. 1. *Schematic of the proposed system.*

Main dimensions of the cavity receiver and tubular reactors are presented in Table 1.

Table 1. *Main dimensions of the cavity and the tubular reactors.*

Tube total height (m)	8.5
Tube inner radius (m)	0.04
Tube outer radius (m)	0.045
Diffusor hole diameter (m)	0.0005
Number of tubes	150
Cavity height (m)	10.5
Cavity width (m)	10
Cavity max. depth (m)	4.5
Aperture height (m)	8.5
Aperture width (m)	5
Aperture area (m^2)	42.5

3. Physical model

The physical behaviour of each tube is represented by a one-dimensional axial model, in which the tube length is discretised into *N* axial segments or nodes. In each axial node, three lumped regions are considered: the SiC tube wall, an two regions corresponding to the tin. A single lumped representation of the molten tin was found to be inadequate according to radial diffusion time. Therefore, the liquid metal was divided into a ring and a core so that the thermal diffusion time of each region is consistent with the transient thermal response induced by variations in the incident solar radiation. Within every node, these regions are assumed radially isothermal, while heat transfer and chemical reaction evolve along the tube axis and in time.

For the purposes of this study, the thermal model is restricted to the operation of the reactor with fully molten tin. It is therefore assumed that the liquid metal is maintained above its melting temperature at all times, for instance by means of an auxiliary heating system or by residual heat storage between operating periods. As a consequence, the initial heating, melting, and solidification of tin during daily start-up and shut-down cycles are not explicitly modelled. The nominal power of the system determines the injected methane mass flow through each tube as follows:

$$\dot{m}_{CH4,in} = \frac{P}{N \cdot \Delta H_{CH4}} \quad (1)$$

The methane risen velocity is calculated from the bubble diameter, D_b, which is primarily influenced by the inner radius of the feeder and the physical properties of the liquid phase. Its estimation can be effectively determined using Tate's law [42]

$$D_b = \left(\frac{6 D_0 \sigma_{tin}}{(\rho_L - \rho_G) \cdot g} \right)^{\frac{1}{3}} \quad (2)$$

where, D_0 is the diffusor holes inner diameter, σ_L is the surface tension of the liquid tin, g is the acceleration due to gravity, ρ_L is the density of the liquid, and ρ_G is the density of methane. With the bubble diameter, the rise velocity is calculated assuming laminar flow conditions due to sequential bubbles formation, through an empirical equation [23]:

$$v_b = 29.69 \cdot {D_b}^{0.316} \quad (3)$$

Therefore, the residence time,τ will be the column height occupied by liquid tin divided by the rise velocity.

$$\tau = \frac{H}{v_b} \quad (4)$$

Because each bubble has a very low density, it is assumed to reach the tin temperature instantaneously [43,44]. Finally, the number of holes on each diffusor element is the volumetric methane flow divided by the risen velocity.

Thermophysical properties of methane were obtained from the NIST database via the CoolProp library and implemented as temperature-dependent functions. For liquid tin and silicon carbide, average thermophysical properties representative of the operating temperature range were adopted from standard materials handbooks. Given the high thermal conductivity of molten tin and the relatively narrow temperature gradients within each axial segment, the use of temperature-averaged properties is considered an acceptable approximation.

In each axial segment, the SiC wall is modelled with a single circumferential temperature, despite the fact that only the aperture-facing sector is directly irradiated. This assumption is supported by a dedicated fin-analysis of the tube cross section, schematically represented in Figure 2.

In that auxiliary model, the irradiated one-third of the perimeter is idealised as a uniform base, while the remaining two-thirds of the circumference act as two circumferential fins with adiabatic tips [45]. Using an effective internal heat transfer coefficient based on the thermal conductivity of liquid tin divided by the tube inner radius, the calculated fin temperature departs by less than 6 °C from the base temperature over a conservative range of base-to-tin temperature differences up to 1200 °C. Such a small angular temperature spread, compared with the absolute operating temperature of the reactor, indicates that the SiC wall behaves as a nearly isothermal ring and therefore justifies adopting a uniform wall temperature around the full circumference in each axial node.

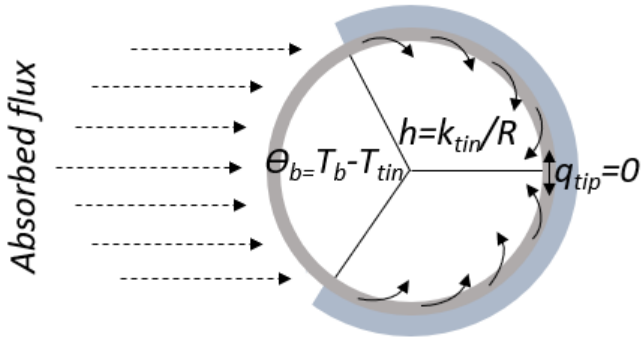

Figure 2. *Thermal analysis of the cross section that model the non-irradiated two thirds of the reactor as fin.*

The energy balance for the SiC region in node j accounts for solar power absorbed on the illuminated external sector, radiative and convective losses to the ambient and conductive heat transfer to the tin ring through the internal surface. The transient wall temperature is obtained from a lumped-capacity equation:

$$(\rho \cdot V \cdot c_p)_{tub} \frac{dT_{tub}}{dt} = q_{solar} - q_{loss} - q_{cond,tube \rightarrow ring} \quad (5)$$

where q_{solar} is the absorbed solar power on the illuminated external sector, q_{loss} accounts for radiative and convective losses to the ambient and $q_{cond,tube \rightarrow ring}$ is the conductive term that couples the wall to the liquid metal.

In the present model, it is assumed that the tin remains fully molten throughout the entire simulated operation. Consequently, phase-change phenomena associated with melting and solidification are not explicitly considered.

The thermal model therefore describes the temperature evolution of liquid tin from its melting temperature up to the high operating temperatures relevant for methane pyrolysis. At relatively low tin temperatures, methane conversion remains negligible as a result of the strong temperature dependence of the reaction kinetics, so that the absence of an explicit solid–liquid transition does not affect the predicted chemical performance.

Under these assumptions, the energy balances for the ring and core regions account only for sensible heat storage in the liquid metal and for conductive heat transfer between the different regions. During operation, the thermal power associated with methane splitting is included as an additional sink term in the energy balances of the ring and core, as described in the following lines:

$$(\rho \cdot V \cdot c_p)_{ring} \frac{dT_{ring}}{dt} = q_{cond,tube \rightarrow ring} - q_{r,ring} - q_{cond,ring \rightarrow core} \quad (6)$$

$$(\rho \cdot V \cdot c_p)_{core} \frac{dT_{core}}{dt} = q_{cond,ring \rightarrow core} - q_{r,core} \quad (7)$$

where q_r represents the thermal power associated with methane splitting in the ring and core regions. Figure 3 schematically depicts all the energy fluxes in the tube wall, ring and core under methane injection conditions.

The thermal power consumed by methane splitting, is calculated from the local kinetics of the reaction and the reactor performance. For the kinetic part, a first-order reaction mechanism is adopted, as commonly reported in the literature for methane pyrolysis [46,47], and the rate constant is expressed with an Arrhenius-type dependence on temperature

$$k(T) = A \cdot e^{\frac{-Ea}{RT}} \quad (8)$$

where *A* is the pre-exponential factor, E_a the activation energy [48], *R* the universal gas constant and *T* the local tin temperature in the corresponding region (ring or core). The reactor performance is described as that of a plug-flow reactor with varying gas density, which is appropriate because the reaction takes place in the gas phase and the stoichiometry changes the total number of moles. In this framework, the rate constant is related to the methane conversion [49]

$$k(T) = \frac{(1+\varepsilon)\cdot \ln\left(\frac{1}{1-0.01\cdot\chi}\right) - \left(\frac{\varepsilon\cdot\chi}{100}\right)}{\tau} \quad (9)$$

where, χ is the methane conversion rate [%] and ε the fractional change in gas volume, that corresponds to 1 in the methane splitting reaction.

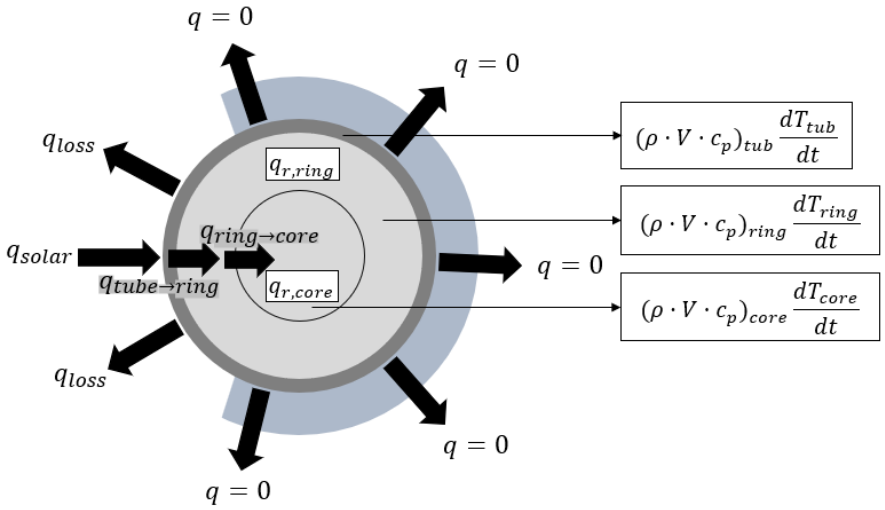

Figure 3. Energy fluxes in the tube wall, ring and core under methane injection conditions

Once *k(T)* and τ are known in a given axial node, this expression provides the outlet conversion χ_{out} from the inlet conversion χ_{in}.The incremental conversion $\Delta\chi = \chi_{out} - \chi_{in}$ determines the mass flow of methane converted in that node:

$$\dot{m}_{out} = \frac{\Delta\chi}{100}\dot{m}_{in} \quad (10)$$

where $\dot{m}_{in}$ is the methane mass flow entering the axial node. Hydrogen production is calculated from the methane conversion at the reactor outlet and the nominal methane mass flow rate, assuming continuous operation and stoichiometric splitting of methane into hydrogen and solid carbon.

The corresponding thermal power of the methane splitting in that region is then:

$$q_r = -\dot{m}_{out} \cdot \Delta H_{CH4} \quad (11)$$

q_{solar} is the solar radiative power is supplied by a heliostat field. For this study, three prescribed axial radiation profiles are analysed: a bell-shaped distribution typical of solar-tower cavity receivers, a uniform distribution used as an ideal reference case, and a more peaked distribution adopted to investigate the impact of stronger axial flux concentrations on reactor behaviour.

Thermal losses from each tube are modelled by assuming that the net heat escaping through the cavity aperture is attributable in equal share to all tubes; thus, the total heat loss through the aperture, divided by the number of tubes, is taken as the thermal loss associated with a single tube.

$$q_{loss} = \frac{A_{ap}}{N} \cdot h_{conv,cav} \cdot (T_{tub} - T_{amb}) + \varepsilon_{cav} \cdot \sigma \cdot \frac{A_{ap}}{N} \cdot (T_{tub}^4 - T_{amb}^4) \quad (12)$$

where $A_{ap}$the external area of the cavity aperture, ε_{cav} is the emissivity of the cavity (taken equal to that of the tubes), and is $h_{conv,cav}$ a representative convective heat transfer coefficient for a non-tilted open cavity [49].

The proposed formulation captures the dominant thermal and chemical phenomena governing reactor operation, while avoiding unnecessary complexity that would obscure the analysis of transient behaviour and solar–reactor interaction.

4. Results

Differently shaped solar distributions, where BS means bell shaped (typical of solar tower plants), F means flat distribution and P means peaked distribution.

Figure 4 compares the three imposed axial solar heat-flux distributions considered in this study: a bell-shaped profile (BS), representative of conventional solar tower cavity receivers, a flat profile (F), used as an idealised reference case, and a peaked profile (P), introduced to assess the impact of strong axial flux concentration. These profiles directly determine the local thermal input to the tubular reactors and therefore govern their transient thermal and chemical response. All solar flux distributions were normalised to deliver the same total thermal power.

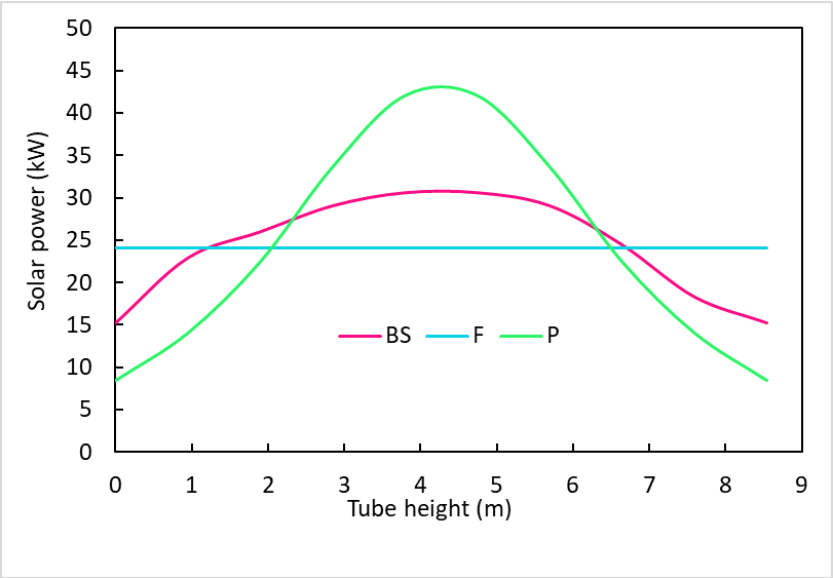

Figure 4. *Axial solar heat-flux distributions studied in this work.*

The resulting temperature evolution at three representative axial locations (bottom, middle, and top nodes of the tube) is shown in Figure 5. For all solar distributions, the temperatures of the SiC tube wall, tin ring, and tin core are virtually indistinguishable, with differences below 1 °C throughout the simulation. This confirms the validity of the radial lumped-capacitance assumption adopted in the model and supports the conclusion that the high thermal conductivity of molten tin ensures an excellent radial thermal homogenisation.

In the case of the bell-shaped distribution, temperatures increase smoothly over time, with the highest values reached in the central axial node, where the absorbed solar flux is maximal. The bottom and top nodes experience slightly lower temperatures, reflecting the reduced local irradiation. This axial temperature profile leads to a moderate but stable methane conversion, as the reaction kinetics are strongly temperature-dependent.

The flat distribution produces a more uniform axial temperature field along the reactor length. As a result, temperature differences between the three axial nodes are minimised, leading to a more homogeneous reaction environment. This configuration reduces local thermal peaks and promotes a steadier methane conversion along the entire tube, which is advantageous from both a materials durability and operational stability perspective.

Conversely, the peaked solar distribution induces sharp temperature elevations in the region of maximum irradiance. This results in significantly higher local temperatures in the middle node, while the lower and upper nodes remain comparatively cooler. Although this configuration enhances the reaction rate locally, it also introduces pronounced axial thermal gradients, which may raise concerns related to thermal stresses in the ceramic tube and non-uniform reaction behaviour.

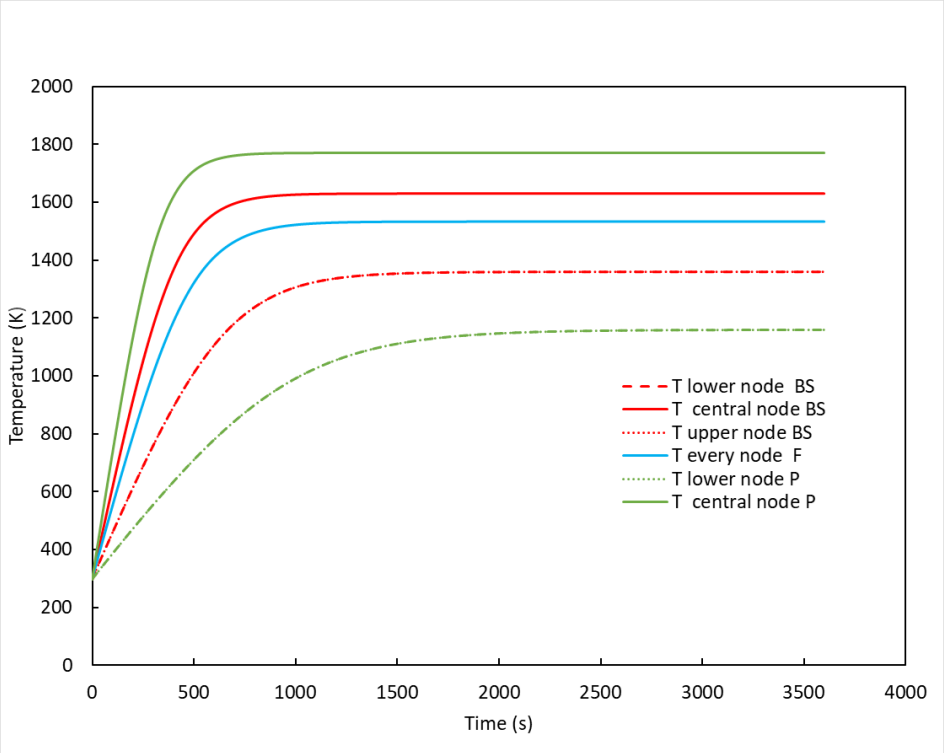

Figure 5. *Axial solar heat-flux distributions studied in this work.*

The implications of these thermal behaviours on hydrogen production are illustrated in Figures 6 and 7. The instantaneous hydrogen production closely follows the temperature evolution within the reactor, exhibiting higher values for configurations that achieve higher average tin temperatures. The peaked distribution yields the highest instantaneous hydrogen production rates due to its elevated local temperatures; however, these rates are more variable over time.

In contrast, the flat distribution leads to a more constant hydrogen production profile, reflecting the uniform thermal conditions inside the reactor. When cumulative hydrogen production is considered, the flat and bell-shaped distributions present comparable overall performance, while the peaked distribution does not provide a proportional increase in cumulative output despite its higher instantaneous peaks. This indicates that extreme axial flux concentration is not necessarily beneficial when integrated over time.

Overall, the results demonstrate that the thermal response of the liquid-tin reactor is highly sensitive to the axial distribution of concentrated solar radiation. The excellent radial thermal homogenisation achieved by the molten metal enables stable operation, while the axial temperature profile dictates methane conversion and hydrogen productivity. Among the configurations analysed, the flat solar flux distribution appears to offer the best compromise between thermal uniformity, stable hydrogen production, and reactor operability, highlighting its potential relevance as a design target for advanced solar receiver systems.

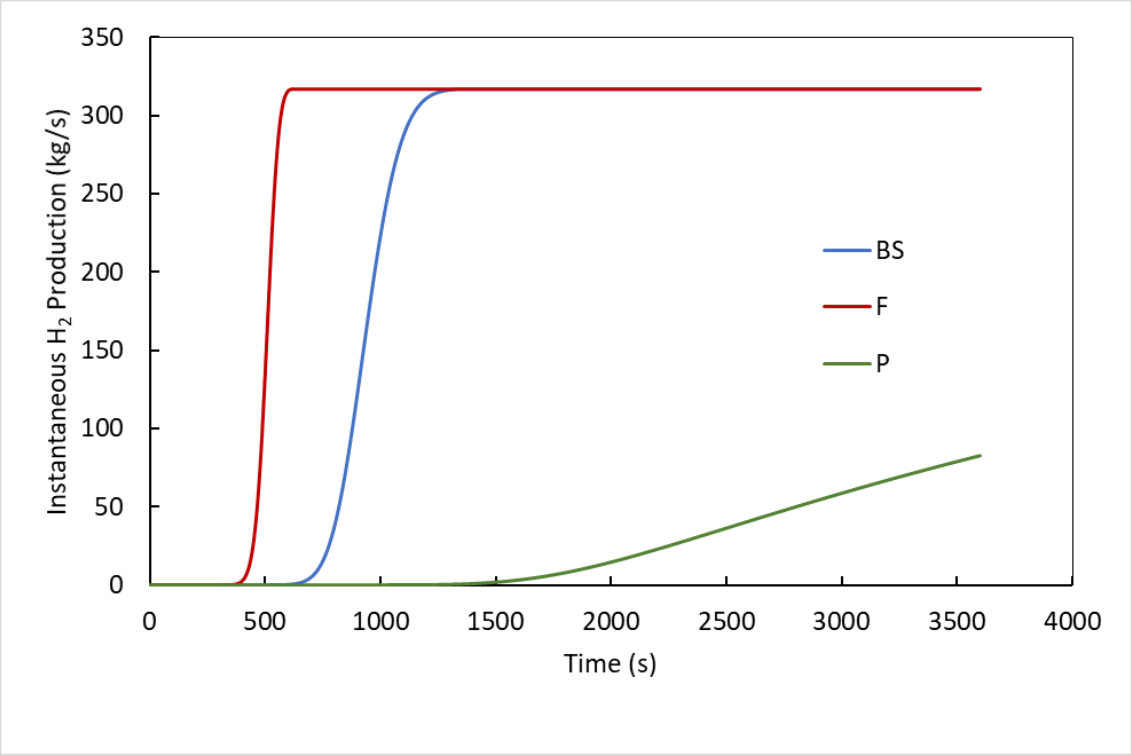

Figure 6. *Instantaneous hydrogen production under the irradiation of the three solar distributions*

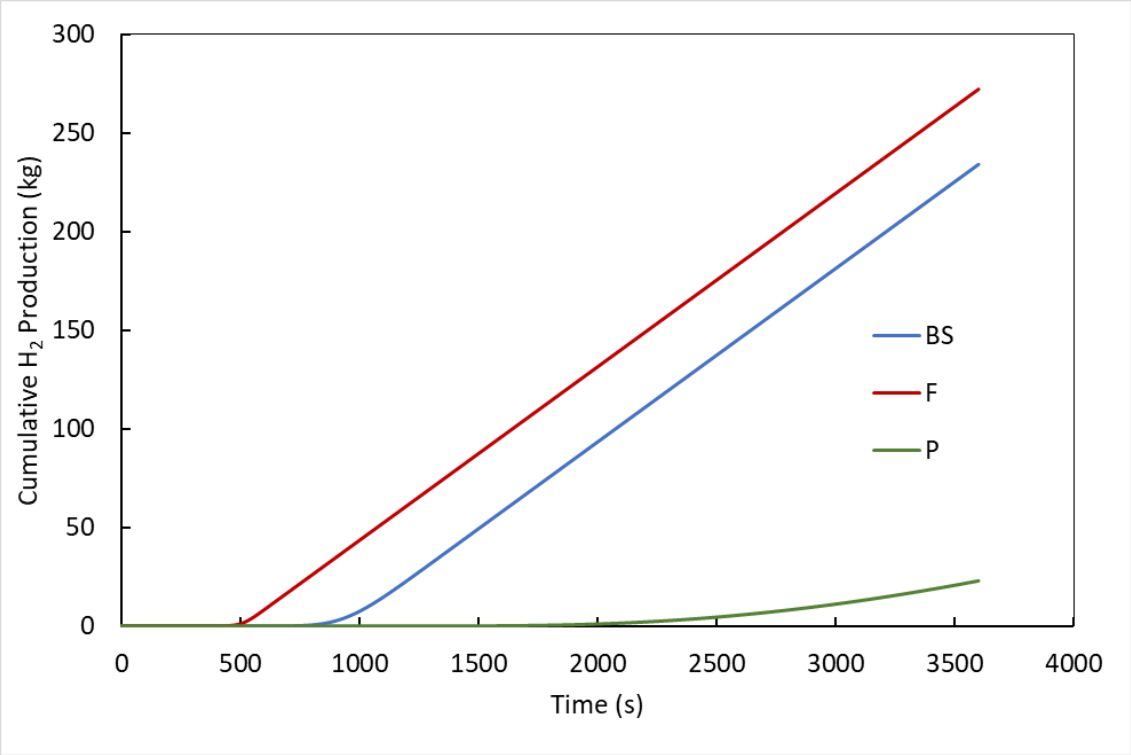

Figure 7. *Cumulative hydrogen production under the irradiation of the three solar distributions*

5. Conclusions

This work presents a transient thermal–reactive modelling framework for a liquid-tin tubular reactor for methane pyrolysis integrated into a concentrating solar tower cavity receiver. The proposed model captures the coupled effects of transient heat transfer, solar irradiation, thermal losses and methane decomposition, providing a physically consistent yet computationally efficient tool for system-level analysis.

The results confirm that molten tin is an effective reaction medium for high-temperature solar methane pyrolysis, as its high thermal conductivity leads to excellent radial thermal homogenisation. This behaviour justifies the use of a lumped radial representation of the liquid metal when appropriate characteristic diffusion times are respected. The subdivision of the tin volume into a ring and a core allows the internal thermal inertia of the metal bath to be captured while maintaining a simplified numerical formulation suitable for transient simulations.

The analysis highlights the strong influence of the axial solar heat-flux distribution on reactor thermal behaviour and hydrogen production. Bell-shaped and flat solar flux profiles promote more uniform axial temperature distributions, resulting in stable methane conversion and smoother hydrogen production rates. In contrast, peaked solar flux distributions generate localised temperature maxima, increasing instantaneous hydrogen production but at the expense of larger axial gradients and higher temporal variability. These effects suggest that excessive axial flux concentration may not be advantageous when overall reactor operability and long-term performance is considered.

From a system perspective, the results demonstrate the technical feasibility of coupling liquid-metal methane pyrolysis reactors with concentrating solar thermal technology for low-carbon hydrogen production. The model provides valuable insight into the interplay between solar flux management, transient thermal response and chemical performance, and can be used to support the preliminary design and optimisation of solar-driven methane pyrolysis systems.

References

[1] Mohammed El-Adawy, Ibrahim B. Dalha, Mhadi A. Ismael, smael ZAA-A, Medhat A. Nemitallah. Review of Sustainable Hydrogen Energy Processes: Production, Storage, Transportation, and Color-Coded Classifications. . Energy & Fuels 2024;38:22686-22718.

[2] Kakran S, Sidhu A, Kumar A, Ben Youssef A, Lohan S. Hydrogen energy in BRICS-US: A whirl succeeding fuel treasure. Appl Energy 2023;334:120670.

[3] Energy Agency I. Global Hydrogen Review 2024. 2024.

[4] Hyogyun Roh, Sehun Oh, Changhyun Lim, Kijung Yong. Recent Progress and Challenges in Hybrid Water Electrolysis through Economic Evaluation. ACS Mater Lett 2024;6:3080–9.

[5] Tyrer Daniel. Production of hydrogen. US1803221A, 1930.

[6] Steinberg M. Production of hydrogen and methanol from natural gas with reduced co, emission. vol. 23. 1998.

[7] M. S. Production of Hydrogen and Methanol from Natural Gas with Reduced CO_2 Emission. Int J Hydrogen Energy, 1998;23:419–25.

[8] M CHCS. Modern and Prospective Technologies for Hydrogen Production from Fossil Fuels. Int J Hydrogen Energy, 1989;14:797-820.

[9] European Commission JRC. European Commission, Critical materials for strategic technologies and sectors in the EU- a foresight study, 2020.

[10] Khoja AH, Azad AK, Saleem F, Khan BA, Naqvi SR, Mehran MT, et al. Hydrogen Production from Methane Cracking in Dielectric Barrier Discharge Catalytic Plasma Reactor Using a Nanocatalyst. Energies (Basel) 2020;13.

[11] Labanca ARDC. Carbon black and hydrogen production process análisis. 45, 25698–25707. Int J Hydrogen Energy 2020;45:25698–707.

[12] Dadsetan M, Latham KG, Khan MF, Zaher MH, Manzoor S, Bobicki ER, et al. Characterization of carbon products from microwave-driven methane pyrolysis. Carbon Trends 2023;12:100277.

[13] Abanades S, Flamant G. Solar hydrogen production from the thermal splitting of methane in a high temperature solar chemical reactor. Solar Energy 2006;80:1321–32.

[14] Rodat S, Abanades S, Sans J-L, Flamant G. Hydrogen production from solar thermal dissociation of natural gas: development of a 10kW solar chemical reactor prototype. Solar Energy 2009;83:1599–610.

[15]Pudukudy M, Yaakob Z. Methane decomposition over Ni, Co and Fe based monometallic catalysts supported on sol gel derived SiO2 microflakes. Chemical Engineering Journal 2015;262:1009–21.

[16]Serrano DP, Botas JA, Pizarro P, Moreno I, Gómez G. Hydrogen production through catalytic methane decomposition promoted by pure silica materials. Int J Hydrogen Energy 2015;40:5237–43.

[17]Nishu, Liu R, Rahman MdM, Sarker M, Chai M, Li C, et al. A review on the catalytic pyrolysis of biomass for the bio-oil production with ZSM-5: Focus on structure. Fuel Processing Technology 2020;199:106301.

[18]Kudinov I V., Velikanova Y V., Nenashev M V., Amirov TF, Pimenov AA. Methane Pyrolysis in Molten Media for Hydrogen Production: A Review of Current Advances. Petroleum Chemistry 2023;63:1017–26.

[19]Geißler T, Plevan M, Abánades A, Heinzel A, Mehravaran K, Rathnam RK, et al. Experimental investigation and thermo-chemical modeling of methane pyrolysis in a liquid metal bubble column reactor with a packed bed. Int J Hydrogen Energy 2015;40:14134–46. https://doi.org/10.1016/j.ijhydene.2015.08.102.

[20]Abánades A, Rathnam RK, Geißler T, Heinzel A, Mehravaran K, Müller G, et al. Development of methane decarbonisation based on liquid metal technology for CO2-free production of hydrogen. Int. J. Hydrogen Energy, vol. 41, Elsevier Ltd; 2016, 8159–67.

[21]Plevan M, Geißler T, Abánades A, Mehravaran K, Rathnam RK, Rubbia C, et al. Thermal cracking of methane in a liquid metal bubble column reactor: Experiments and kinetic analysis. Int J Hydrogen Energy 2015;40:8020–33.

[22]Zhang Y, Cai Y, Hwang SH, Wilk G, DeAngelis F, Henry A, et al. Containment materials for liquid tin at 1350 °C as a heat transfer fluid for high temperature concentrated solar power. Solar Energy 2018;164:47–57.

[23]Andreini RJ, Foster JS, Callen RW. Characterization of gas bubbles injected into molten metals under laminar flow conditions. Metallurgical Transactions B 1977;8:625–31.

[24]Zaghloul N, Kodama S, Sekiguchi H. Hydrogen Production by Methane Pyrolysis in a Molten-Metal Bubble Column. Chem Eng Technol 2021;44:1986–93.

[25]Abánades A, Rubbia C, Salmieri D. Thermal cracking of methane into Hydrogen for a CO2-free utilization of natural gas. Int. J. Hydrogen Energy, vol. 38, 2013, p. 8491–6.

[26]Abánades A, Rubbia C, Salmieri D. Technological challenges for industrial development of hydrogen production based on methane cracking. Energy 2012;46:359–63.

[27]Romero M, Steinfeld A. Concentrating solar thermal power and thermochemical fuels. Energy Environ Sci 2012;5:9234.

[28]Arias I, Cardemil J, Zarza E, Valenzuela L, Escobar R. Latest developments, assessments and research trends for next generation of concentrated solar power plants using liquid heat transfer fluids. Renewable and Sustainable Energy Reviews 2022;168:112844.

[29]'Gus' Nathan GJ, Lee L, Ingenhoven P, Tian Z, Sun Z, Chinnici A, et al. Pathways to the use of concentrated solar heat for high temperature industrial processes. Solar Compass 2023;5:100036.

[30]Abuseada M, Spearrin RM, Fisher TS. Influence of process parameters on direct solar-thermal hydrogen and graphite production via methane pyrolysis. Int J Hydrogen Energy 2023;48:30323–38.

[31]Zeng K, Gauthier D, Li R, Flamant G. Solar pyrolysis of beech wood: Effects of pyrolysis parameters on the product distribution and gas product composition. Energy 2015;93:1648–57..

[32] Msheik M, Rodat S, Abanades S. Experimental comparison of solar methane pyrolysis in gas-phase and molten-tin bubbling tubular reactors. Energy 2022;260..

[33]Cundr O, Haladova D. Original Research Article Biogas Yield from Anaerobic Batch Co-Digestion of Rice Husk and Zebu Dung. Agricultura Tropica et Subtropica 2014;46:118–22.

[34]Moset V, Poulsen M, Wahid R, Højberg O, Møller HB. Mesophilic versus thermophilic anaerobic digestion of cattle manure: methane productivity and microbial ecology. Microb Biotechnol 2015;8:787–800.

[35]Gómez-Quiroga X, Aboudi K, Álvarez-Gallego CJ, Romero-García LI. Successful and stable operation of anaerobic thermophilic co-digestion of sun-dried sugar beet pulp and cow manure under short hydraulic retention time. Chemosphere 2022;293:133484.

[36]Mojapelo N, Muzenda E, Kigozi R, Aboyade AO. Bio-methane Potential of the Organic Fraction of Municipal Solid Waste . 6th Int'l Conf. on Green Technology, Renewable Energy & Environmental Engg. (ICGTREEE'2014), Cape Town: 2014.

[37]Rasi S, Veijanen A, Rintala J. Trace compounds of biogas from different biogas production plants. Energy 2007;32:1375–80.

[38]Khawer MU Bin, Naqvi SR, Ali I, Arshad M, Juchelková D, Anjum MW, et al. Anaerobic digestion of sewage sludge for biogas & biohydrogen production: State-of-the-art trends and prospects. Fuel 2022;329.

[39]Tjutju NAS, Ammenberg J, Lindfors A. Biogas potential studies: A review of their scope, approach, and relevance. Renewable and Sustainable Energy Reviews 2024;201:114631.

[40]Westerholm M, Liu T, Schnürer A. Comparative study of industrial-scale high-solid biogas production from food waste: Process operation and microbiology. Bioresour Technol 2020;304:122981.

[41]Vidal A, Gonzalez A, Denk T. A 100-kW cavity-receiver reactor with an integrated two-step thermochemical cycle: Thermal performance under solar transients. Renew Energy 2020;153:270–9.

[42]Kulkarni AA, Joshi JB. Bubble Formation and Bubble Rise Velocity in Gas−Liquid Systems: A Review. Ind Eng Chem Res 2005;44:5873–931.

[43]Plevan M, Geißler T, Abánades A, Mehravaran K, Rathnam RK, Rubbia C, et al. Thermal cracking of methane in a liquid metal bubble column reactor: Experiments and kinetic analysis. Int J Hydrogen Energy 2015;40:8020–33.

[44]Geißler T, Plevan M, Abánades A, Heinzel A, Mehravaran K, Rathnam RK, et al. Experimental investigation and thermo-chemical modeling of methane pyrolysis in a liquid metal bubble column reactor with a packed bed. Int J Hydrogen Energy 2015;40:14134–46.

[45]Gallo A, Spelling J, Romero M, González-Aguilar J. Preliminary Design and Performance Analysis of a Multi-megawatt Scale Dense Particle Suspension Receiver. Energy Procedia, vol. 69, Elsevier Ltd; 2015, p. 388–97.

[46]Becker T, Richter M, Agar DW. Methane pyrolysis: Kinetic studies and mechanical removal of carbon deposits in reactors of different materials. Int J Hydrogen Energy 2023;48:2112–29.

[47]Abánades A, Ruiz E, Ferruelo EM, Hernández F, Cabanillas A, Martínez-Val JM, et al. Experimental analysis of direct thermal methane cracking. Int J Hydrogen Energy 2011;36:12877–86.

[48]Alonso E. Gallo A, Abánades A.Techno-economic analysis of (bio)methane pyrolysis in liquid tin driven with concentrating solar thermal . 14th National and 5th International Conference on Engineering Thermodynamics (CNIT); Zaragoza: 2025.

[49]Houssainy S, Janbozorgi M, Kavehpour P. Thermodynamic performance and cost optimization of a novel hybrid thermal-compressed air energy storage system design. J Energy Storage 2018;18:206–17.